Reverberation Mapping Analysis of the 2016 HST Campaign on NGC 4593

Lukas Diehl

George-August-Universität Göttingen

November 21, 2025

Abstract

Abstract

Contents

List of Figures

List of Tables

1. Introduction

Active galactic nuclei (AGN) are among the most luminous objects in the universe, emitting radiation across the entire electromagnetic spectrum (Netzer 2013). Unlike inactive galaxies like the Milky Way, the supermassive black-hole (SMBH) in an active galaxy continues to accrete matter from its central region. This process generates thermal radiation (Peterson 1997) as well as non-thermal emission such as photoionization and subsequent recombination (Netzer 2013). While the central AGN region is not directly resolvable, analyzing its spectral features allows constraints on the kinematics, geometry, and physical conditions of the central region. Owing to the intrinsic variability of AGNs, time lags can be measured between the light curves of different spectral features in the spectrum, particularly between the continuum emission from the accretion disk and the responding broad emission lines of the broad-line region. By combining these time delays with the observed widths of the emission lines, the mass of the SMBH can be estimated. This technique is known as reverberation mapping (RM) (Peterson 1993).

A representative example of this class of objects is the AGN of the active barred spiral galaxy NGC 4593, which shows strong variability from the X-ray to the optical bands (McHardy et al. 2017). To perform a reverberation mapping analysis an observation campaign over several days or weeks is needed, to measure the variability of NGC 4593. For this purpose, a monitoring campaign with the Hubble Space Telescope (HST) was used, which was conducted by E. M. Cackett (Cackett et al. 2018).

Based on this campaign, the goal if this thesis will be a classical reverberation mapping analysis of NGC 4593, with a particular focus on spectral features like the optical broad emission lines such as the Balmer emission lines. An additional focus will be on the variability and time lag of the O$\textsc{i}\,\lambda 8446$ emission line, which may be strengthened by a Bowen fluorescence process (Bowen 1947; Netzer and Penston 1976). This is of particular interesting, because the measurement of O$\textsc{i}\,\lambda 8446$ variability as well as its lag in NGC 4593 from a RM campaign has not be done before.

2. Scientific Background

2.1 Active Galactic Nuclei

Active Galactic Nuclei (AGN) refer to the central region of active galaxies. Those objects are among the most luminous objects in the universe, with bolometric luminosities ranging from 10^{41} to 10^{48} erg s^{-1}, outshining entire galaxies by several orders of magnitude (Peterson 1997). Over the years, several stellar-powered models were proposed, such as dense star clusters or supermassive stars. However, these scenarios were discarded, as they are expected to collapse into black holes themselves, and they cannot provide the required energy output (Rees 1984). Today, it is understood that the enormous luminosities of AGN are powered by accretion of matter onto a supermassive black hole (SMBH) at their centers (Rees 1984). The most widely accepted model for this accretion is a hot, rotating accretion disk surrounding the SMBH, which produces most of the observed radiation (Shakura and Sunyaev 1973). The following sections will outline the key components of an AGN, introduce the unification model that connects various AGN types, and summarize common classification schemes. A special focus will be on AGN variability, which plays a central role in the reverberation mapping analysis conducted in this thesis.

Figure 2.1: Different components of an AGN. Adopted from (Mo et al. 2010) Figure 14.3.

5

2.1.1 Structure and Spectral Features of an AGN

Figure 2.1 shows a schematic structure of an AGN, consisting of a central supermassive black hole (SMBH), a surrounding accretion disk, a dusty torus, and ionized gas regions known as the broad-line region (BLR) and narrow-line region (NLR). In some cases, relativistic jets are launched perpendicular to the plane of the accretion disk (Urry and Padovani 1995). The following subsections describe the intrinsic structures of AGN and the spectral features associated with them.

Supermassive Black Hole and Accretion Disk

The center of an AGN is formed by a supermassive black hole (SMBH), with typical masses between $10^6 \, M_\odot$ and $10^9 \, M_\odot$ (Peterson et al. 2004). It does not contribute to the AGN spectrum by itself, but acts as the central engine for all observed spectral features of the AGN. It dominates the gravitational potential and other then inactive Galaxies, like the milky-way, it is surrounded by an accretion disk. Due to viscosity processes within the disk, like turbulent friction or magneto-rotational instability, the angular momentum of the matter is getting transported further out of the disk, which leads to a spiraling matter flow inwards the SMBH (Shakura and Sunyaev 1973). Several models have been proposed to describe the accretion process. The most widely used one is the geometrically thin and optically thick accretion disk, consisting of ionized gas in differential rotation around the SMBH (Netzer 2013). The disk is composed mainly of ionized hydrogen and helium, with traces of heavier elements (Netzer 2013). It extends from the innermost stable circular orbit (ISCO) near the event horizon out to distances of several light-days. The radial extent of the disk is relatively small compared to galactic scales and typical ranges from a few light-hours to a few light-days, corresponding to about 10^{-3} to 10^{-2} pc (Shakura and Sunyaev 1973; Netzer 2013).

During the accretion process a significant fraction of the gravitational energy of the matter is transformed into thermal radiation, which accounts for the enormous luminosity observed in AGNs and heats the accretion disk up to very high temperatures depending on the size of the SMBH (Netzer 2013). As an example, the maximum effective temperature for an accretion disk around a SMBH with $M = 10^8, M_\odot$ is on the order of several $\times 10^5$ K, leading to UV and optical emission (Shakura and Sunyaev 1973; Netzer 2013). In comparison, disks around stellar-mass black holes reach much higher temperatures (up to a few $\times 10^6$ K), emitting mostly in X-rays (Shakura and Sunyaev 1973; Netzer 2013). Due to the radial temperature gradient, the emitted spectrum cannot be described as a single black body. Instead, it results

from a combination of many black-body-like components at different temperatures, often referred to as a multi-color black-body (Netzer 2013). This produces a broad optical–UV continuum of ionizing photons, which interact with gas clouds near the nucleus and play a crucial role in shaping the spectral features of the BLR and NLR. These photons cause photoionization followed by recombination, which leads to to the strong emission lines that are characteristic of AGN spectra (Netzer 2013).

Broad-Line and Narrow-Line Region

The ionized gas clouds near the nucleus can be divided into the broad-line region (BLR) and the narrow-line region (NLR). Both regions differ in density, distance from the SMBH, and observed line widths (Urry and Padovani 1995). The BLR is located close to the nucleus at distances of a few light-days to a few light-years from the central SMBH (Goad et al. 2012)(see Figure 2.1). It consists of dense gas clouds with electron densities of $n_e \approx 10^{11}\,\text{cm}^{-3}$, moving at high velocities of several thousand $\text{km}\,\text{s}^{-1}$ due to the strong gravitational influence of the SMBH. These velocities lead to a significant Doppler broadening of permitted emission lines with widths of $(500\text{–}10{,}000)\,\text{km}\,\text{s}^{-1}$ (Peterson 1997). As described earlier, the BLR is photo-ionized by the continuum radiation emitted from the accretion disk. Consequently, the line emission from this region responds to changes in the continuum, leading to a strong correlation between both and shows strong variation (Netzer 2013). This relationship is particularly relevant for reverberation mapping, which will be discussed later in Section 2.2.

To model the geometry of the BLR is a challenging task, as several emission lines have to be considered, which vary in their intensities due to changes in the variable continuum radiation (Netzer 2013). A common model assumes a spherical distribution of clouds that is connected to the accretion disk and located between the accretion disk and the dusty torus (Goad et al. 2012). Broad emission lines appear in permitted transitions such as Hα, Hβ and Lyα. (Netzer 2013)

Up to several hundred parsecs from the central region lies the narrow-line region (NLR) (Peterson 1997). The gas in this region moves at much lower velocities, resulting in emission lines with widths typically in the order of $(350-400)$ km s^{-1}(Peterson 1997). In contrast to the BLR, the NLR allows both permitted and forbidden transitions. Forbidden lines, such as [O III] $\lambda5007$, arise because collisional de-excitation is inefficient at the relatively low densities of the NLR ($n_e \sim 10^2\text{–}10^4\text{cm}^{-3}$) (Peterson 1997). Due to its much larger extends, compared to the BLR, the NLR responds only very slowly to variations in the ionizing continuum. Following that, the flux

of the narrow emission lines can be seen as constant over the time scales of several years (Peterson 1993). Therefore, narrow lines can be used to intercalibrate the spectra of the various observations employed in this thesis. In this work, the narrow [O III] $\lambda5007$ line was used for intercalibration (see Chapter 3).

Dusty Torus

Surrounding the accretion disk and broad-line region is the dusty torus, a geometrically thick and optically dense structure composed of gas and dust. It extends from a radius, where dust can survive the intense radiation of the accretion disk, out to scales of a few parsecs (Netzer 2013). The torus likely has a clumpy distribution and plays a crucial role in the unified model of AGNs which will be discussed in a later section (Urry and Padovani 1995; Netzer 2013). The dust in the torus absorbs a significant fraction of the UV and optical radiation emitted by the accretion disk and re-emits it thermally in the infrared. As a result, AGNs typically exhibit strong infrared emission, with the peak wavelength depending on the temperature of the dust in the torus (Netzer 2013). Even in cases where the central region is hidden from direct view by the torus, this reprocessed infrared emission remains observable. It therefore provides a characteristic signature of obscured AGN activity and enables indirect constraints on the otherwise hidden central region (Netzer 2013).

2.1.2 Classification

AGNs get classified in subgroups based on their spectral features, which are strongly dependent to their intrinsic structure. The key parameters for this classification are luminosity, emission-line profiles and radio properties. Based on those parameters AGN get grouped into Seyfert galaxies, quasars and radio galaxies. They get further subdivided based on the appearance of broad and narrow emission lines. Some examples for these sub-classes are narrow-line Seyfert I galaxies (NLS1s), low-ionization nuclear emission-line regions (LINERs), and jet-dominated sources such as BL Lac objects or blazars (Antonucci 1993; Urry and Padovani 1995).

Seyfert Galaxies

Seyfert galaxies are named after Carl K. Seyfert, who in 1943 observed spiral galaxies characterized by exceptionally bright nuclei and strong emission lines in their optical spectra (Seyfert 1943). They are mainly classified into the sub-classes Seyfert I and Seyfert II based on the presence of broad emission lines. Figure 2.2 highlights the differences of the spectra of Type I and Type II Seyfert galaxies.

Figure 2.2: An example of Seyfert I and Seyfert II spectra illustrating their differences. Broad lines, such as the highlighted $H\alpha$ and $H\beta$, are only present in the Seyfert I spectrum, whereas forbidden [O III] lines are visible in both cases. Adopted from (Runco 2015). **Ursprüngliche quelle nicht nachvollziebar. BRauch etwas anderes**

Seyfert I galaxies, such as NGC 4593, show both broad and narrow emission lines in their optical spectra. The broad lines, such as $H\alpha$ and $H\beta$, typically have full widths at half maximum (FWHM) of several thousand kilometers per second and from the fast-moving, high-density gas in the BLR (Peterson 1997). In contrast, narrow lines, including prominent forbidden transitions like [O III] $\lambda 5007$ or [N II] $\lambda 6584$, originate from the slow-moving, low-density gas in the NLR (Peterson 1997). The presence of both components in the spectrum allows for a clear classification as a Seyfert I galaxy, which is the case for NGC 4593. Further details on NGC 4593 are provided in Section 3.1. Between the two main Seyfert classes, several intermediate subclasses (1.2, 1.5, 1.8, 1.9) are defined based on the ratio of the broad towards the narrow components in the optical spectrum (Osterbrock 1977; Osterbrock 1981; Peterson 1997). Seyfert 1.8 and 1.9 galaxies show very weak broad components. In Seyfert 1.9 objects, the broad component is visible only in the Hα line, whereas in Seyfert 1.8 objects it is also detectable in Hβ. Furthermore, if the broad and narrow components in Hβ are of equal strength, the AGN is classified as a Seyfert 1.5 (Peterson 1997). If the narrow component is even weaker than

the broad component, it is classified as a Seyfert 1.2 (Osterbrock 1977). The fact that the optical spectrum shows multi-component lines with both broad and narrow components, suggests that these emission lines originate in the BLR and the NLR in the respective ratio (Peterson 1997).

In comparison, Seyfert II galaxies completely lack these broad components in their optical spectra, likely due to orientation-dependent obscuration by the dusty torus. Following that the classification of a Seyfert galaxies strongly depends on the viewing angle of the observer, which is the key point for the Unified Model of AGN, which will deepened in section 2.1.3 (Peterson 1997).

Another notable subclass is the group of so-called narrow-line Seyfert I galaxies (NLS1s). They show most of the features of Seyfert 1 or 1.5 galaxies, except that the usually broad lines, such as the H I or He I lines, exhibit FWHM values that are only slightly larger than those of the narrow lines. They show a wide dispersion of spectral properties, with some objects have very strong Fe II emission, whereas others show almost none. This indicates that NLS1s do not form a homogeneous class (Osterbrock and Pogge 1985). NLSls are thought to have low-mass black holes accreting at high Eddington rates, suggesting they may represent a young evolutionary phase of AGN activity(Peterson 2011; Netzer 2013). Another possible explanation is an orientation effect. Another possible explanation is an orientation effect. When an NLS1 is observed at a very low inclination, the projected velocities are reduced, which leads to smaller observed Doppler broadening and therefore to narrow lines (Osterbrock and Pogge 1985).

Additional AGN Classes

In addition to Seyfert galaxies, there are several other classes of AGN. Quasars, which stands for quasi-stellar radio sources, are even more luminous than Seyfert galaxies and are typically found at higher redshifts. While the host galaxies of Seyfert galaxies are still observable, quasars completely outshine their host galaxies. Since quasars show similar emission characteristics to Seyfert galaxies, the modern distinction is based mainly on luminosity: quasars are classified as high-luminosity AGNs, while Seyfert galaxies represent the lower-luminosity end (Netzer 2013).

Radio galaxies form another important AGN class, distinguished by their strong radio emission and prominent jets, typically found in elliptical host galaxies. When their jets are aligned close to our line of sight, they are observed as blazars or BL Lac objects, which exhibit rapid variability and featureless optical spectra due to relativistic beaming (Netzer 2013).

Finally, LINERs are low-luminosity AGNs with spectra dominated by low-ionization

emission lines. The physical origin of their ionization mechanism is still debated, and in some cases, they may not be powered by accretion at all (Netzer 2013).

While these classifications are based primarily on spectral characteristics, many of the observed differences between AGN types can be attributed to orientation effects. The Unified Model of AGN provides a framework that explains this apparent diversity through a common internal structure, viewed from different angles.

2.1.3 Unification Model

Figure 2.3 shows an illustration of the Unification Model, which was postulated by Robert Antonucci in 1993. He proposed that the visible differences in AGN spectra are not due to fundamentally different structures. Instead, they arise mainly from the viewing angle toward the AGN center and from obscuration by the dusty torus (Antonucci 1993).

The figure shows with what type the same AGN would get classified depending on the observers viewing angle. Like mentioned before, the dusty torus plays a key role here, as it surrounds the central region of the AGN, the accretion disk and the fast-moving BLR. If the observer's line of sight is blocked by the torus, only radio emission, the optical/UV continuum and narrow-line emission from the NLR outside the torus can be detected. In this case, the AGN is classified as a Seyfert 2 galaxy, as the broad emission lines originating from the BLR are obscured and the optical/UV continuum from the accretion disk is only partially visible. The observer essentially views the AGN from a flat angle, looking directly at the torus.

If, on the other hand, the observer has a direct view into the central region of the AGN, not obscured by the torus, the fast moving gas clouds of the BLR as well as the optical/UV emission continuum from the accretion disk become visible. In this case, both broad and narrow emission lines are visible, meaning the AGN is classified as a Seyfert 1 galaxy. (Urry and Padovani 1995).

The same principle applies to other AGN classes. Quasars can be considered the high-luminosity counterparts of Seyfert galaxies, where orientation and torus obscuration likewise affect their observed properties. Blazars, on the other hand, are seen when the relativistic jet is aligned closely with the observer's line of sight, leading to strong Doppler boosting, which makes the radiation appear significantly brighter and shifted to higher frequencies than it intrinsically is (Urry and Padovani 1995). Although the classical Unification Model treats AGN classification as fixed and purely geometry-driven, some AGNs have been observed to change their spectral type over time (Ricci and Trakhtenbrot 2023). These so-called "changing-look

AGNs" demonstrate that a purely orientation-based interpretation, such as the Unification Model, cannot explain all observed phenomena. They suggest that intrinsic changes, such as variations in accretion rate or obscuring material, can also affect the classification (Ricci and Trakhtenbrot 2023).
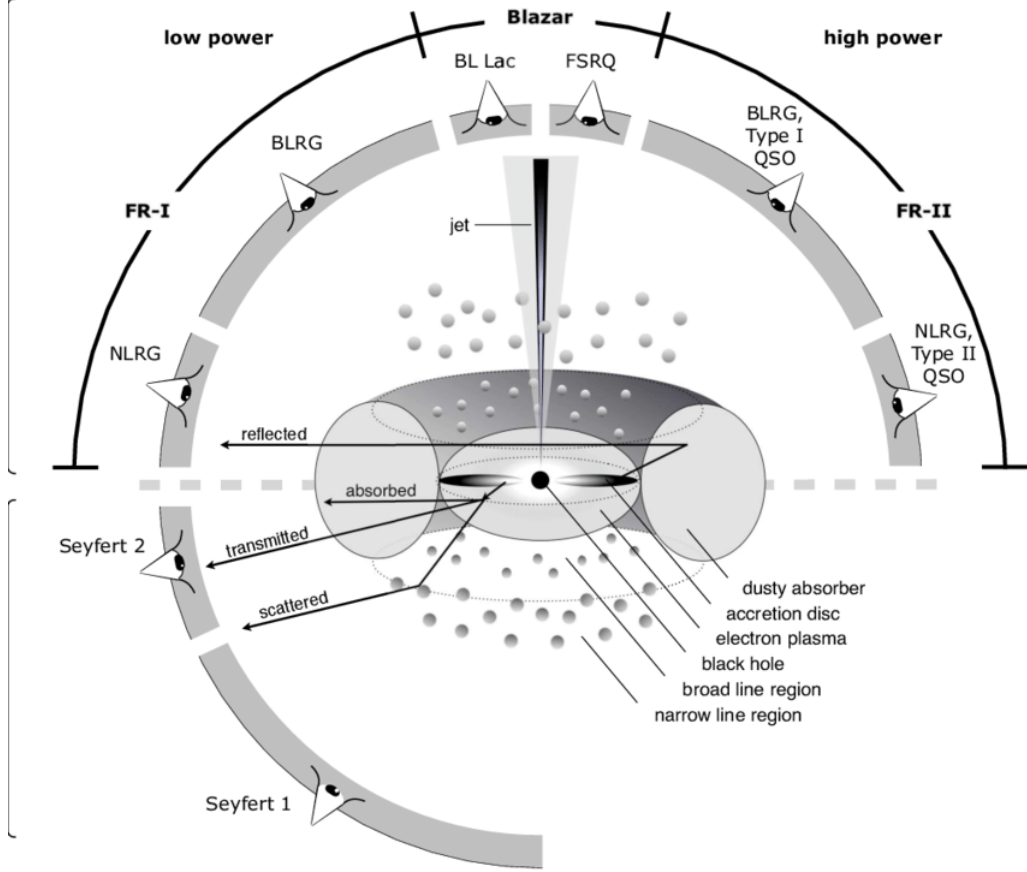
Figure 2.3: This graphic shows a schematic of the unification model of an AGN. The figure was adopted from (Beckmann and Shrader 2013).

2.1.4 Variability

The variability of active galactic nuclei (AGN) is one of the key aspects that enables the study of their central regions, which generally cannot be probed with classical spatially resolved methods. Variability is observed on timescales from hours to several years and generally shows stochastic behavior, resulting in flux variations of both emission lines and continuum emission of up to a few tens of percent in the UV and optical regimes (Ulrich et al. 1997; Ochmann et al. 2024). While the origin of this variability is not yet fully understood, the most widely accepted models attribute it to inhomogeneities and instabilities within the accretion disk (Ulrich et al. 1997; Dexter and Agol 2010).

Depending on the physical process, the variations occur on different characteristic timescales. Processes such as thermal fluctuations or changes in the accretion flow act on timescales of decades to centuries for typical SMBH masses and radii, and are therefore difficult to observe directly. In contrast, processes operating on shorter timescales are much easier to study. Examples of such processes are gas motions and mechanical instabilities, such as sound waves, within the disk, which occur on timescales of weeks to months (Ricci and Trakhtenbrot 2023). The shortest timescale is the light-crossing timescale, $t_{\mathrm{lc}} = R/c$, which specifies how long light takes to traverse the variable emitting region, such as the broad-line region (BLR) (Ricci and Trakhtenbrot 2023). Here, c denotes the speed of light and R describes the characteristic size or radius of the variable emitting region. Following Ricci and Trakhtenbrot 2023, by assuming a SMBH of mass $\approx 10^8\, M_\odot$, the light-crossing timescale can be written as

$$t_{\mathrm{lc}} = \frac{R}{c} \simeq 0.87 \left(\frac{R}{150\, r_g} \right) M_8 \,\text{days,} \qquad (2.1)$$

where $r_g = GM/c^2$ denotes the gravitational radius of the black hole. It follows that the light-crossing timescale of the variable emitting regions is on the order of days, and that t_{lc} scales linearly with the size of the emitting region (Ricci and Trakhtenbrot 2023).

Because variations in the ionizing continuum occur on such short timescales, it is possible to measure delayed responses from other correlated regions within the AGN using long-term monitoring campaigns (Peterson 1997). In particular, the BLR responds to changes in the photoionizing continuum radiation of the central source with a time delay or lag that is bigger than the light-crossing timescale of the emitting region (Peterson 1997). This time lag forms the basis of a classical reverberation mapping analysis, which will be further elaborated in the next section.

2.2 Reverberation Mapping

The main focus of this work is a classic reverberation mapping analysis of the broad lines of NGC 4593. This observational technique allows to probe the structure of the BLR around the SMBH inside the AGN. This technique bases on the time delay or time lag between the continuum's variation and the correlated response of the broad lines. With this calculable time lag it is possible to infer the geometry of the BLR and to calculate the mass of the SMBH (Cackett et al. 2018).

2.2.1 Principle of Reverberation Mapping

The fundamental assumption in reverberation mapping is that variation in the observed continuum's flux corresponds to the variation in the emission-line flux, with a measurable time delay. With variation in the continuum luminosity, the emission-line response follows these continuum variations with a measurable time lag (Cackett et al. 2021).
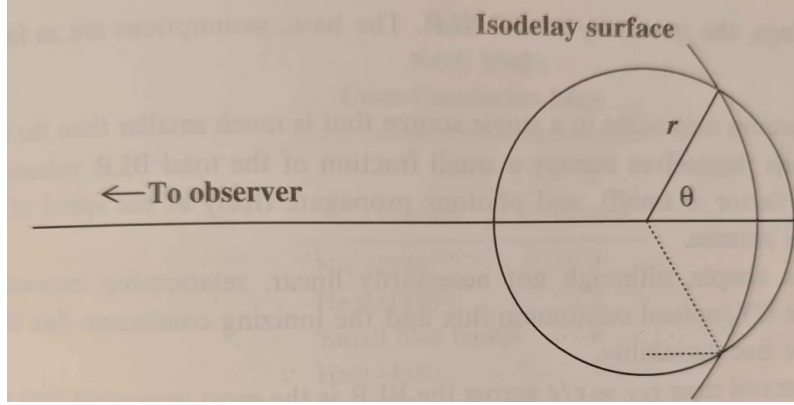

Figure 2.4: Spherical distribution model of the broad line region and isodelay surface, adopted from (Peterson 1997).

This time lag τ is corresponding to the average light-travel time from the photoionization continuum to the line emitting regions. Taking the idealized model for the BLR as spherical distributed clouds (Goad et al. 2012), then τ can be assumed as (Peterson 1997)

$$\tau = (1 + \cos\theta) \cdot \frac{R_{\mathrm{BLR}}}{c}, \qquad (2.2)$$

where R_{BLR} is the characteristic size or radius of the BLR, c the speed of light and θ the angle of the BLR from the line of sight of the observer to the central source (2.4) (Peterson 1997). The circle in Figure 2.4 describes the spherical distribution of the BLR. For a fixed lag τ the location for the responding emitting region must lay on a paraboloid, that fits to the observers line of sight to the continuum, which is called the isodelay surface. Following that the position of the BLR, that is emitting with the fixed lag τ has to be located on the intersection of the BLR distribution and the isodelay surface (Peterson 1997). Thus, reverberation mapping can be used to 'map' the BLR's structure by infer the characteristic radius of the BLR from the time lag (Peterson 1997). But because the observer sees not one, but all possible isodelay surfaces that a possible for a fixed lag τ, the so called 'transfer equation' is

14

needed which integrates over all isodelay surfaces (Peterson 1997):

$$L(t) = \int \Psi(\tau) C(t - \tau) d\tau \qquad (2.3)$$

$\Psi(\tau)$ refers to the transfer function, delivering the BLR's geometric and kinematic information, $C(t)$ refers to the contiuuum light curve and $L(t)$ the emission light curve (Peterson 1997). While in theory the response of the BLR can be fully described by the transfer function $\Psi(\tau)$, this lag can be estimated using cross-correlation techniques. In practice, recovering the full transfer function $\Psi(\tau)$ would require very well-sampled and high signal-to-noise light curves over a duration much longer than the expected lag. Since real monitoring campaigns are often affected by observational gaps and noise, such reconstructions are rarely possible (Horne et al. 2004; Peterson 1993). For this reason, this thesis concentrates on measuring the mean time lag between continuum and emission-line variations using the interpolated cross-correlation function (ICCF) method (Gaskell and Peterson 1987).

2.2.2 Lag Measurement

Using the notation from Peterson 1997 the cross-correlation function between the ionizing continuum and an emission line is defined as

$$F_{\text{CCF}}(\tau) = \int_{-\infty}^{\infty} L(t)C(t - \tau)dt, \qquad (2.4)$$

With the auto-correlation function of the ionizing continuum

$$F_{\text{ACF}}(\tau) = \int_{-\infty}^{\infty} C(t)C(t - \tau)dt \qquad (2.5)$$

and the transfer equation 2.3, the cross-correlation function can be written as the convolution of the transferfunction and the auto-correlation function of the ionizing continuum:

$$F_{\text{CCF}}(\tau) = \int_{-\infty}^{\infty} \Psi(\tau')F_{\text{ACF}}(\tau - \tau')d\tau' \qquad (2.6)$$

The lag is defined to be at the location of the peak (τ_{peak}) or the centroid (τ_{centroid}) of the CCF (Peterson 1997). While τ_{peak} is defined as the peak of the CCF, τ_{centroid} gets calculated over all points of the CCF, which are above a selected threshold which is typically 80%. Because of the strong relation of the CCF and the transferfunction, it is possible to infer a scale length for the BLR, where the emission line originated from (Peterson 1997), which can be describe with $R_{\text{BLR}} = c \cdot \tau_{\text{centroid}}$ using the light-

travel time scale (Peterson et al. 2004). Since the centroid lag is generally considered a more robust representation of the mean light-travel time of the BLR (Peterson et al. 2004), it is used in this thesis.

The uncertainty of the measured lag is estimated using a monte varlo approach combining flux randomization (FR) and random subset selection (RSS) (Peterson et al. 2004). In the FR step, each flux value is randomly perturbed according to its measurement uncertainty. In the RSS step, a subset of the data points is drawn at random with replacement, preserving the original sample size. For each realization, the ICCF analysis is repeated, resulting in a distribution of centroid lags. The median of this distribution is adopted as the final lag measurement, while the 16th and 84th percentiles are taken as the 1σ confidence interval, accounting for both measurement noise and the effects of uneven temporal sampling.

2.2.3 Black-Hole Mass

With the measured rest-frame centroid lag τ_{centroid} from the ICCF analysis and the velocity width of the broad emission line, the mass of the central supermassive black hole (SMBH) can be estimated under the assumption that the BLR gas is gravitationally bound and its motions are dominated by the SMBH potential (Peterson et al. 2004). The distance to the BLR is given by

$$R_{\mathrm{BLR}} = c \cdot \tau_{\mathrm{centroid}} \tag{2.7}$$

and, combined with the line-of-sight velocity dispersion ΔV of the BLR gas, the virial product is defined as:

$$M_{\mathrm{vir}} = \frac{R_{\mathrm{BLR}} \, \Delta V^2}{G}. \tag{2.8}$$

The physical black hole mass is then obtained by applying a scale factor f, which accounts for the unknown geometry, kinematics, and inclination of the BLR:

$$M_{\mathrm{BH}} = f \cdot M_{\mathrm{vir}}. \tag{2.9}$$

Following Onken et al. (2004), a mean value of f is adopted, calibrated by aligning reverberation-based masses with the $M_{\mathrm{BH}} - \sigma_*$ relation observed in not-active galaxies. Here, σ_* describes the stellar velocity dispersion of the galactic bulge. The actual scale factor can still vary between individual AGN because of differences in their geometry and orientation, which results in systematic uncertainties in the SMBH mass estimation. Still, the calibration of f against $M_{\mathrm{BH}} - \sigma_*$ delivers a

well-established methode for estimation the SMBH mass and will be used in this thesis.

2.3   Bowen Fluorescence

The mechanism known as Bowen Fluorescence was first described by I.S. Bowen in 1934 to explain unexpected emission lines in nebular spectra. This mechanism describes a resonant line pumping process, where Photons emitted by an ion, hits randomly another ion of a different species with a matching permitted transition, and excites it via absorption due to a near-wavelength coincidence. The resulting de-excitation leads to an enhancement of the emission lines (Bowen 1934).

One transition that can be enhanced by Bowen fluorescence is the O$\textsc{i}\lambda$8446 emission line, which is pumped by Lyβ fluorescence (Netzer and Penston 1976). In this process, Lyβ photons at $\lambda 1025.72\,\text{Å}$ are absorbed by neutral oxygen through the near-resonant transition $2p^4\,^3P_2 \rightarrow 3d\,^3D^0$ of O $\textsc{i}$ at $\lambda 1025.77\,\text{Å}$. The excited $3d\,^3D^0$ level decays to $3p\,^3P$, which then decays to $3s\,^3S^\circ$, emitting the O $\textsc{i}\,\lambda$8446 emission line (see figure 2.5) (Grandi 1980). This adds another possible contributing excitation mechanism to the O$\textsc{i}\lambda$8446 emission line, in addition to recombination. **evtl noch erweitern**
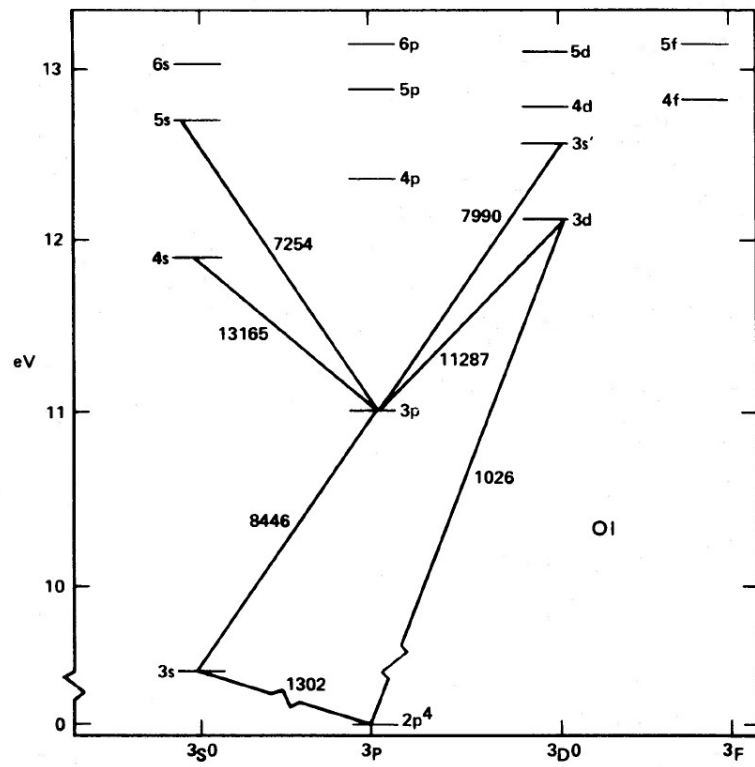
Figure 2.5: Energy level diagram of the triplet states of OI, adopted from (Grandi 1980).

3. Campaign and Data Preparation

The analysis of this campaign is based on the observation campaign of NGC4593 in 2016 by Cackett et al. 2018. This campaign took place between the 12th of July and the 6th of August with daily observations, which resulted in 26 successful out of 27 observations. It was performed with the Hubble Space Telescope (HST) using the Space Telescope Imaging Spectrograph (STIS) with the three different Gratings. The following section will cover an overview of the properties and specifications of NGC4593 and the campaign in 2016.

3.1 NGC4593

NGC 4593 is an active galactic nucleus (AGN), classified as a Seyfert 1 galaxy with a (R)SB(rs)b barred spiral morphology. It is located in the southern sky at RA = 12:39:39.44, DEC = $-05°20'39.03''$ (J2000) and has a redshift of $z = 0.0083 \pm 0.0005$, corresponding to a distance of about 35.6 Mpc (SIMBAD 2025) based on the ΛCDM model. The galaxy exhibits a prominent large-scale bar and nuclear dust ring connected to dust lanes along the bar, which likely channel gas toward the central region (Mulchaey and Regan 1997), as seen in figure 3.1. ALMA observations, conducted by (Garcia-Burillo et al. 2019), reveal a central molecular gas reservoir of $\sim 10^8$ $M_\odot$ arranged in a one armed spiral and a circumnuclear ring, as well as evidence for a mild molecular outflow on scales of a few hundred parsecs, highlighting the interplay between a bar driven inflow and an AGN feedback in this galaxy.

The AGN of NGC4593 shows strong broad emission lines in Hα, Hβ, Hγ, Lyα, He I, and He II (Bentz and Katz 2015), indicating a well-developed broad-line region. It has a apparent magnitude of $B = 13.95$ mag and $V = 13.15$ mag (Véron-Cetty and Véron 2010) which gives a color index of $(B - V) = 0.80$ mag. Near-infrared photometry shows emission as well in the J, H, and K bands with $J = 8.96 \pm 0.02$ mag, $H = 8.29 \pm 0.02$ mag, and $K = 7.98 \pm 0.03$ mag (Skrutskie and al. 2006), illustrating the broad spectral energy distribution emitted by the AGN.
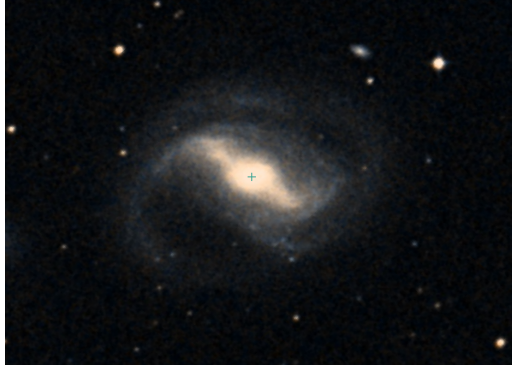
Figure 3.1: A DSS image of NGC4593.

Earlier reverberation mapping campaign based these broad lines showed a supermassive black hole mass of about $M = (7.63 \pm 1.62) \times 10^6 \, M_\odot$ (Bentz and Katz 2015), which corresponds to a broad-line region radius of only a few light-days (Denney et al. 2006). Furthermore NGC4593 shows strong variability from X-ray to optical bands, with time delays that indicate a UV/optical-emitting accretion disk about three times larger than predicted by standard thin-disk theory and signatures of diffuse continuum emission from the BLR (Cackett et al. 2018).

3.2 The 2016 Hst Campaign

The Cackett et al. 2018 campaign was designed to study wavelength dependent continuum lags. Therefore, the STIS instrument on the Hubble Space Telescope was used with low-resolution gratings to measure a broad range of wavelengths. In each observation, spectra were taken using three different gratings: G140L, G430L, and G750L. These were used together with the $52'' \times 0.2''$ slit.

The characteristics of the STIS gratings used in this analysis are summarized in Table 3.1. After a standard pipeline-processing, a package was used to do a Charge Transfer Inefficiency correction with an algorithm based on (Anderson and Bedin 2010). The few left rest of hot pixels got manually removed by interpolating the flux of neighbor pixels.

Table 3.1: Overview of STIS Grating Characteristics (Space Telescope Science Institute 2025)

Grating	Range [Å]	Exp. Time [s]	Res. Power	Dispersion [Å/pixel]
G140L	1119–1715	1234	~ 1000	0.6
G430L	2888–5697	298	$\sim 500 - 1000$	2.73
G750L	5245–10233	288	$\sim 500 - 1000$	4.92

3.3 Intercalibration and Determination of AVG and RMS Spectra

Reverberation mapping requires multiple epochs to capture variability. For the 2016 campaign of NGC 4593, we retrieved 27 spectra from the ... archive of which 26 are usable for further analysis. The top panel of Figure 3.2 shows a section between about 4000 Å and 9000 Å of the optical spectral range from these epochs.

For the subsequent analysis, the average spectrum (AVG) is obtained by averaging over all epochs. Ideally, this improves the signal-to-noise ratio (S/N) sufficiently to identify spectral features in NGC 4593. Furthermore it is essential for the reverberation mapping analysis to identify variability between the epochs, which can be obtained with the root-mean-spuare (RMS) spectrum, defined as the standard deviation of the flux at each wavelength across epochs:

$$F_{\mathrm{RMS}}(\lambda) = \sqrt{\frac{1}{N-1} \sum_{i=1}^{N} \left[F_i(\lambda) - \bar{F}(\lambda) \right]^2}, \qquad (3.1)$$

with the mean spectrum at wavelength λ given by

$$\bar{F}(\lambda) = \frac{1}{N} \sum_{i=1}^{N} F_i(\lambda). \qquad (3.2)$$

Constant features, like narrow emission lines, vanishes in the RMS spectrum, whereas variable components, like broad emission lines stands out. The top panel of Figure 3.2 shows the AVG and RMS spectra from the original retrieved data. It showes, that residual variability remains in nominally non-varying lines, especially in the forbidden features near 5000 Å. This indicates small wavelength misalignment between epochs. Therefore an intercalibration anchored to the narrow [O III] $\lambda 5007$ line was performed, by correcting the wavelengths of the spectra by a maximum of 1Å. The lower panels of Figures 3.2 present the intercalibrated epochs and the corresponding AVG and RMS spectra. The disappearance of narrow features in the calibrated RMS spectrum, especially the [O III] $\lambda 5007$ line, confirms that the apparent variability in the uncalibrated RMS was induced by the wavelength shifts between the epochs rather than intrinsic line variability. However the intercalibration was only applied to the optical part of the spectra due to its limited reliability. Following that the intercalibrated AVG and RMS spectra will be used for optical part, taken by the G430L and G750L gratings used in the following analysis and the uncalibrated AVG and RMS spectra for the emission lines in the UV part of

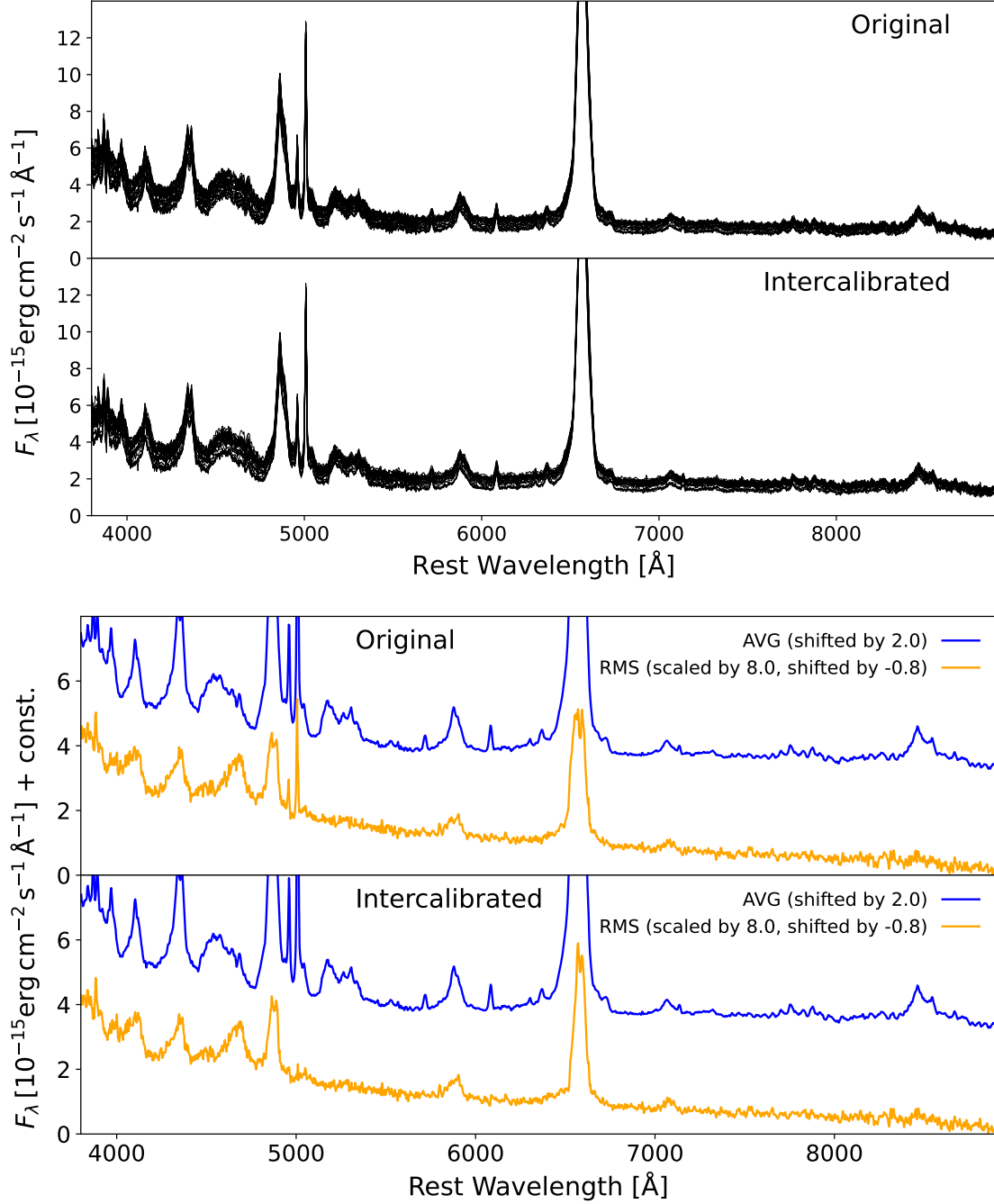spectrum and their analysis, as they were taken by the G140L gratings.

Figure 3.2: Comparison of the spectral range between 4000Å and 9000Å from the 2016 HST campaign of NGC 4593, showing the effects of [O III] λ5007 intercalibration on both the individual spectra (top) and the derived average and rms spectra (bottom).

4. Reverberation Mapping Analysis of NGC4593

4.1 Line Identification

Having obtained the AVG- and RMS spectrum of NGC4593, the next step is the identification of the emission lines. Figures 4.1 and 4.2 show the optical to near-infrared range between 3900Å and 9000Å and the UV range between 1100Å and 1700Å, respectively.
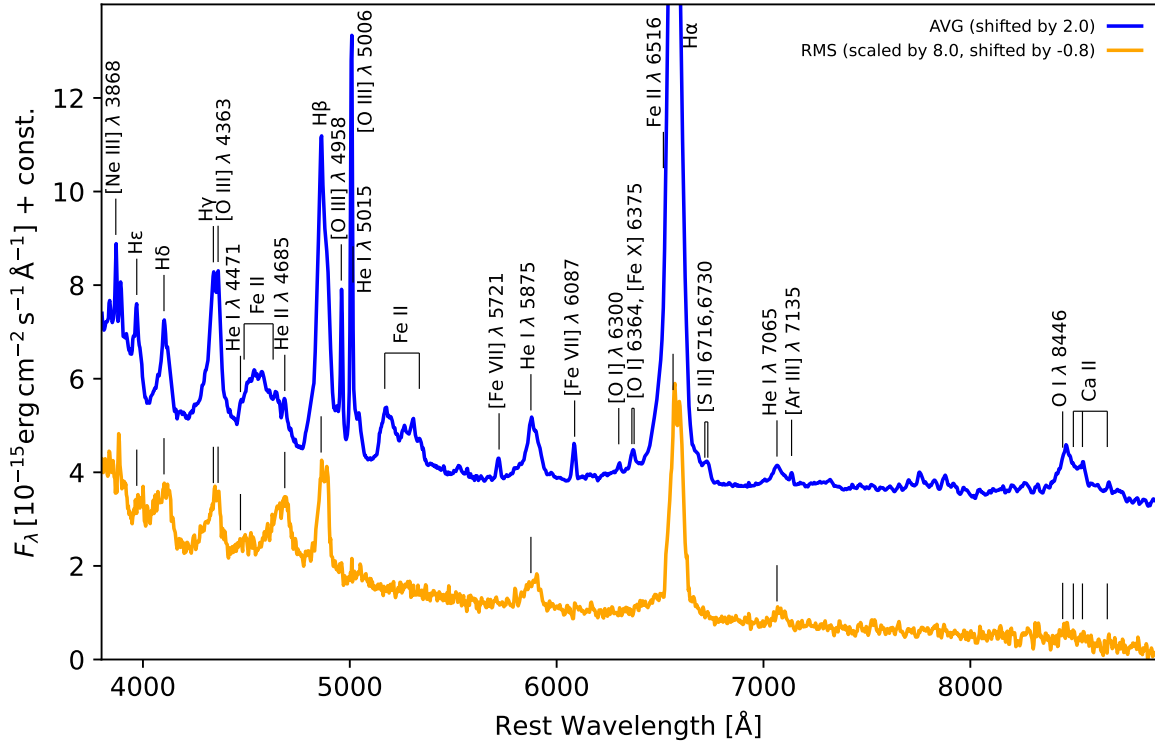

Figure 4.1: Optical-to-NIR AVG and RMS spectrum with identified emission lines.

Looking at Figure 4.1, the most prominent broad emission lines in the AVG spectrum are the Balmer-Lines, with Hα being the strongest followed by Hβ and Hγ. Their variations are clearly visible in the RMS spectrum and the line profiles of Hα and Hβ in particular show strong similarities, which will be discussed in more detail later in this chapter. In addition to the Balmer emission lines there are several He-emission lines such as He II λ4685, He I λ5875 and He I λ7065 show measurable variability. Another significant broad emission line complex appears in the NIR part of the spectrum, including the O I λ8446 and Ca II lines. The O I λ8446 line is of particular interest in this thesis, as it shows variation which was never measured through a reverberation mapping analysis before.

Apart from the broad emission lines, the AVG spectrum also exhibits several strong forbidden emission lines with the [O III] λ5007 and the [O III] λ4958 as the most prominent ones. As mentioned in the previous chapter, the first one was used for the intercalibration of the spectra and, as expected, shows no variability in the RMS spectrum, similar to the other forbidden lines. Finally, the AVG spectrum shows additionally two Fe II emission line groups, that shows no variation in the RMS spectrum.
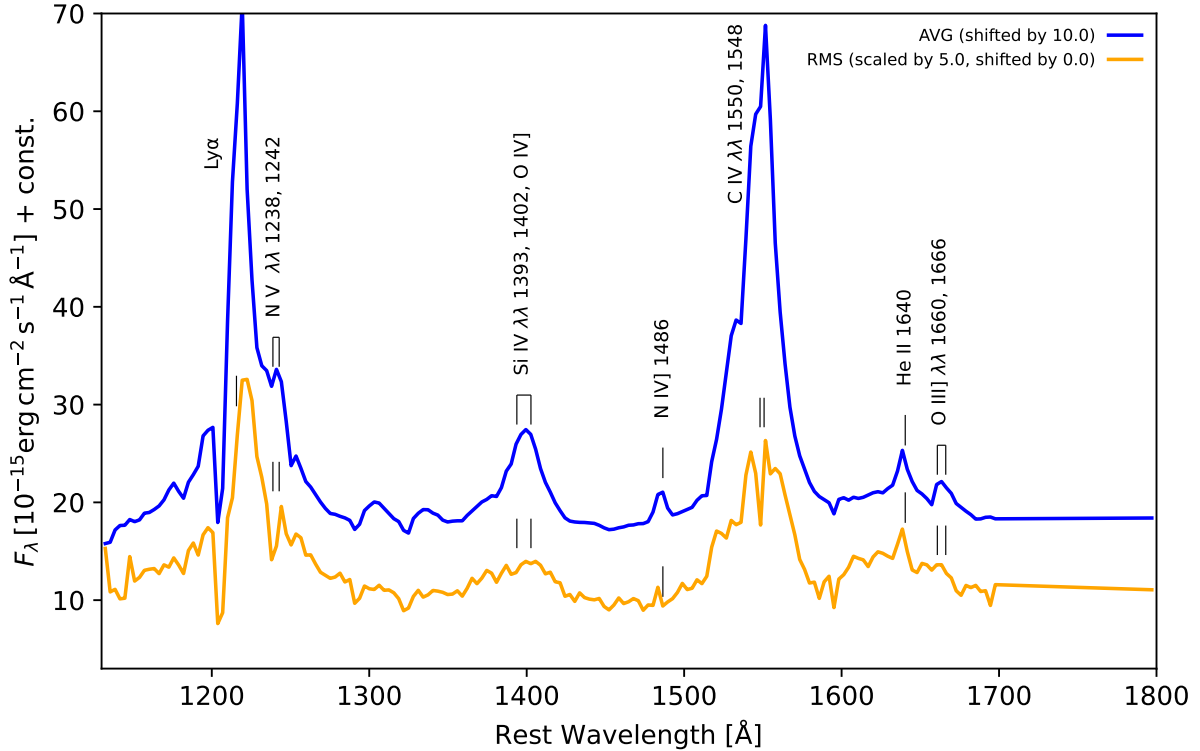

Figure 4.2: UV spectrum AVG and RMS spectrum with identified emission lines

The UV spectrum, shown in figure 4.2, contains only a few additional broad and semi-forbidden emission lines due to its limited coverage. In addition to the prominent Si and C broad emission lines, it shows strong and variable Ly_α emission, which is of particular significance for this thesis.

The Bowen fluorescence of O I $\lambda 8446$, which is investigated in this analysis, is typical driven by the emission of the $Ly\beta$ line, which lies outside the spectral range of the HST Campaign. However, as can be seen in figure 4.2, $Ly\alpha$ still lies in the spectral range of the campaign, as the most blue broad line of the taken spectra. As Ly_α and Ly_β are assumed to originate from the same physical region, Ly_α can be used to examine the correlation of O I $\lambda 8446$ and $Ly\alpha$ for Bowen fluorescence.

4.2 Emission Line and Continua Measurement

After identifying the emission lines, the next step of the analysis is to calculate the fluxes of those lines. This is done with the help of a python-based tool called gecho, which uses methods for lag measurements and line-width measurements based on ... . With help of this tool the flux density gets integrated over the extent of each emission line for every observed spectrum of the campaign. Here it is important to define the integration limits so that only the variable component of the emission line is measured in this way To ensure this, a parallel view of the AVG- and RMS-spectrum was used to define those integration limits, by identifying the variable components of the line in the RMS-spectrum. Additionally, it must be ensured, that no component of any other line is contributing to the line flux of the measured line, which can lead to misleading conclusions. But before the line flux can be calculated, the surrounding continuum has to be subtracted, which can be done by interpolating a linear pseudo-continuum between sections on the blue and red side with no line contribution. The chosen integration limits and pseudo-continua can be found in Table 4.1. With the fluxes of each line now derived from all observed spectra, it is possible to extract the lightcurves of the measured emission line, which will be further covered in the next section.

Besides the emission line lightcurves, continua lightcurves from different wavelength ranges are needed for the further analysis. The extraction process is similar to the emission line lightcurves, except that they get calculated by the mean flux density of a sufficiently large region without line emission or absorption. Logically a pseudo-continua subtraction is not needed here. The chosen integration limits for the continua can be found in Table 4.2.

Table 4.1: Integration Limits and Pseudo-Continua of the measured emission lines

Line	Integration Limits	Pseudo-Continua
Lyα	$1207 - 1238$	$1151 - 1161, 1462 - 1468$
Hα	$6520 - 6634$	$6107 - 6129, 6861 - 6900$
Hβ	$4828 - 4924$	$4762 - 4774, 5085 - 5112$
Hγ	$4317 - 4391$	$4197 - 4220, 4435 - 4450$
HeI $\lambda5875$	$5840 - 5941$	$5645 - 5653, 6044 - 6057$
HeII $\lambda4685$	$4610 - 4744$	$4435 - 4450, 4762 - 4774$
OI $\lambda8446$	$8380 - 8498$	$8005 - 8031, 8850 - 8955$
OIII $\lambda5007$	$4982 - 5033$	$4762 - 4774, 5085 - 5112$

Table 4.2: Integration Limits of the measured continua

Line	Integration Limits
Cont. 1150	$1151 - 1161$
Cont. 4010	$4026 - 4033$
Cont. 4440	$4435 - 4450$
Cont. 5100	$5085 - 5112$
Cont. 6110	$6107 - 6129$
Cont. 6880	$6861 - 6900$
Cont. 8015	$8005 - 8031$
Cont. 8900	$8864 - 8955$

The variability of the emission lines and continua being the basis of a reverberation analysis, it is helpful to use variability statistics, as defined by Rodriguez-Pascual et al. 1997. Thus include the extrema of the flux densities of the emission lines as well as the extrema of the integrated fluxes of the continua $F_{\min}$ and $F_{\max}$, the ratio of the maximum and minimum flux $R_{\max}$, the mean flux $\langle F \rangle$, the standard deviation σ_F and finally the fractional variation, which is defined as:

$$F_{\text{var}} = \frac{\sqrt{\sigma_F^2 - \Delta^2}}{\langle F \rangle} \tag{4.1}$$

Here Δ^2 is the mean square value of the uncertainties of the fluxes defined as:

$$\Delta^2 = \frac{1}{N} \sum_N^{i=1} \Delta_i^2 \tag{4.2}$$

The results of these parameters can be found in table 4.3.

Table 4.3: Variability statistics of the investigated continua and broad lines with minimum (2) and maximum flux density or integrated flux (3), peak-to-peak ratio (4), mean (5), standard deviation (6) and fractional variation (7).

Continuum/Line (1)	$F_{\min}$ (2)	$F_{\max}$ (3)	$R_{\max}$ (4)	$\langle F \rangle$ (5)	σ_F (6)	F_{var} (7)
Cont. 1150	0.52	1.35	2.58	0.86	0.25	0.28
Cont. 4010	2.68	4.21	1.57	3.49	0.47	0.14
Cont. 4440	2.42	3.73	1.54	3.14	0.39	0.12
Cont. 5600	1.36	2.15	1.59	1.82	0.25	0.14
Cont. 6110	1.49	2.27	1.53	1.9	0.23	0.12
Cont. 6880	1.33	2.01	1.5	1.72	0.2	0.11
Cont. 8015	1.18	1.69	1.43	1.48	0.15	0.1
Cont. 8900	1.14	1.52	1.33	1.38	0.11	0.08
Lyα	66.87	94.88	1.42	82.21	8.03	0.1
Hα	112.34	129.72	1.15	122.03	4.36	0.04
Hβ	32.7	39.12	1.2	36.49	1.77	0.05
Hγ	14.45	17.85	1.24	16.5	0.94	0.06
HeII $\lambda 4685$	5.53	9.81	1.77	7.73	1.37	0.18
HeI $\lambda 5875$	6.81	9.54	1.4	8.49	0.62	0.07
OI $\lambda 8446$	7.47	9.13	1.22	8.32	0.37	0.04
OIII $\lambda 5007$	12.97	13.65	1.05	13.39	0.18	0.01
UVW2	-	-	-	-	-	0.125

4.3 Lightcurves

This chapter will cover the plots and comparison of the extracted emission line and continua lightcurves. Additionally to the measured lightcurves, the UVW2 continuum lightcurve from the swift campaign taken by (McHardy et al. 2018) is included in the further analysis, as it was used by E. Cackett in his analysis too (Cackett et al. 2018).

4.3.1 Continua

First looking at the continua lightcurves in figure 4.3, it shows that they follow a similar overall shape. All lightcurves start with a pronounced maxima, which shows in most cases the highest flux level, with exception of the 1150 continuum. This is followed by a significant flux minimum where the flux decreases by about $25 - 46\%$ relative to the total flux maximum of the curve. From there the curves rise again toward another local maximum that nearly reaches the initial peak. In most

cases, this second maximum is composed of a higher plateau, a smaller plateau, and an additional peak, before the lightcurves steadily decline toward their overall flux minimum.

Describe the selection of the Cont. 1015 continuum and the UVW2 continuum

4.3.2   Emission Lines

Like mentioned earlier, the lightcurves of the emission-lines Hα, Hβ, Hγ, Lyα, HeI λ5875, HeII λ4685 and OI λ8446 where selected for the further reverberation mapping analysis. Figure 4.4 and 4.5 show those lightcurves compared to the selected blue continuum Cont. 1150 and respectively compared to the external swift continuum UVW2. This comparison shows strong similarities between the continua and emission-line lightcurves, as most features of the 1150 and UVW2 continuum lightcurves can be found in the emission-line curves too, shifted within a few days.

create comparison figures for this lightcurves
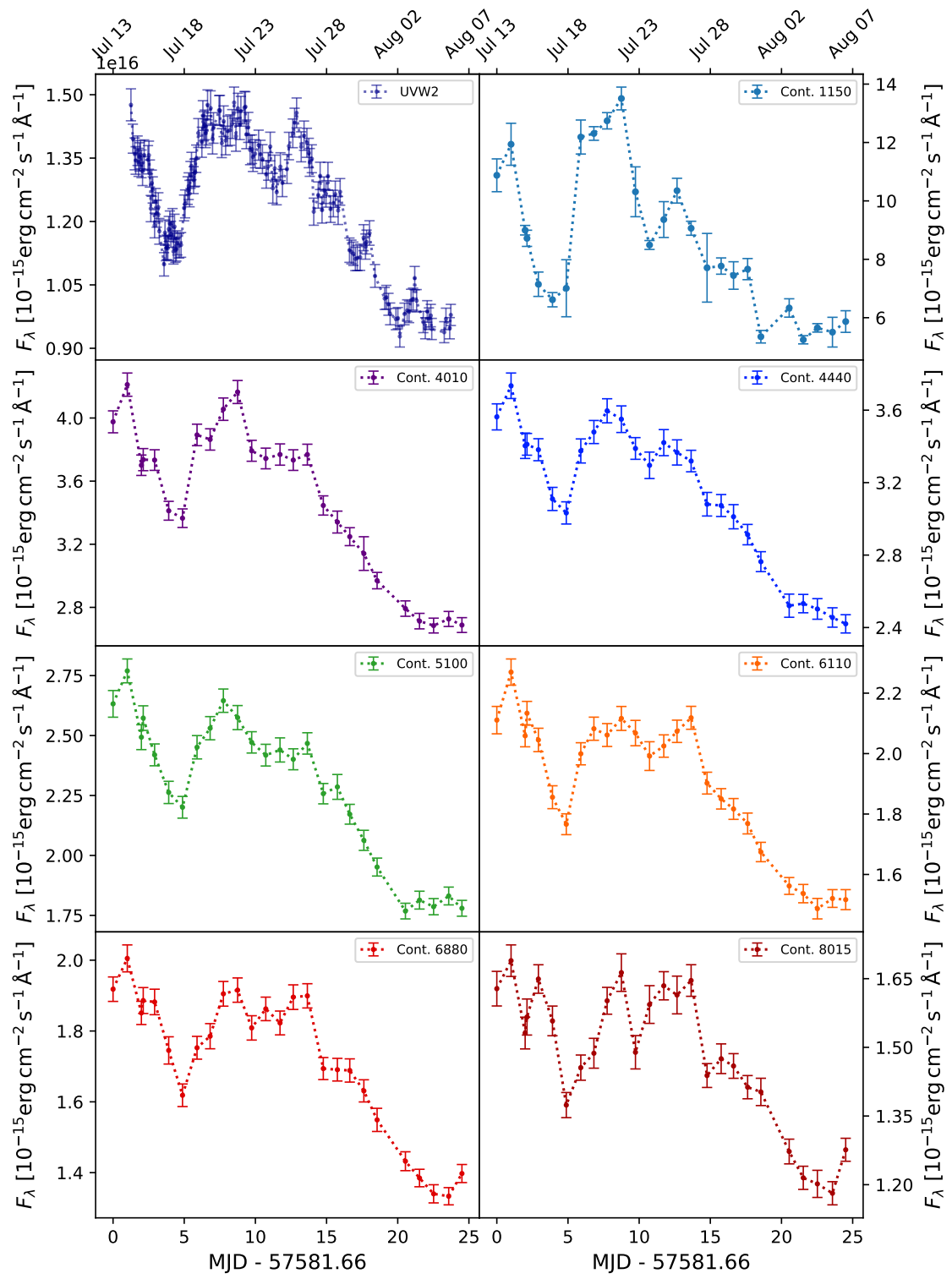
4.4   Line Profiles
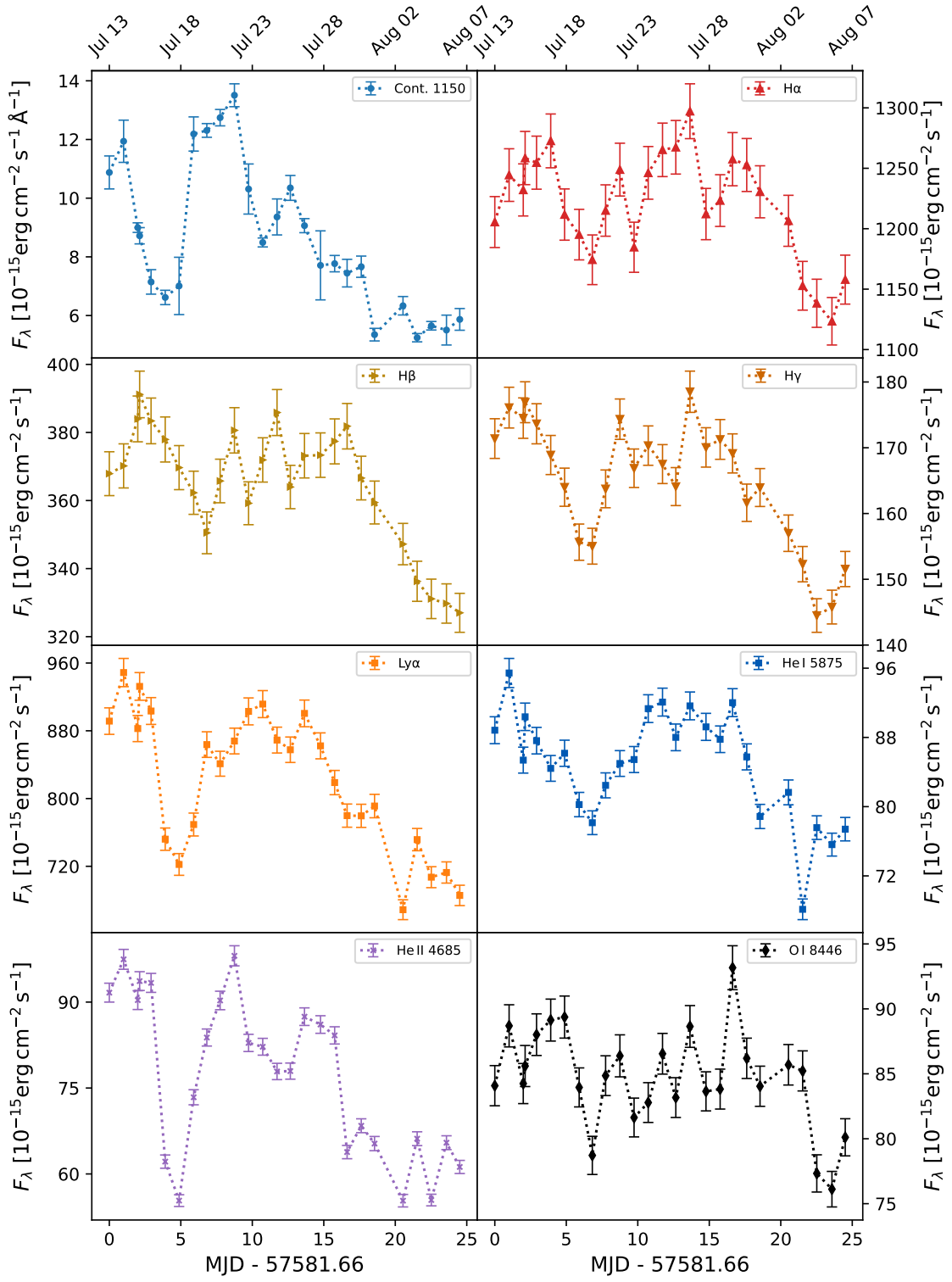
4.5   Time Lag and BH Masses

Figure 4.3: ...

Figure 4.4: AVG RMS Spektrum
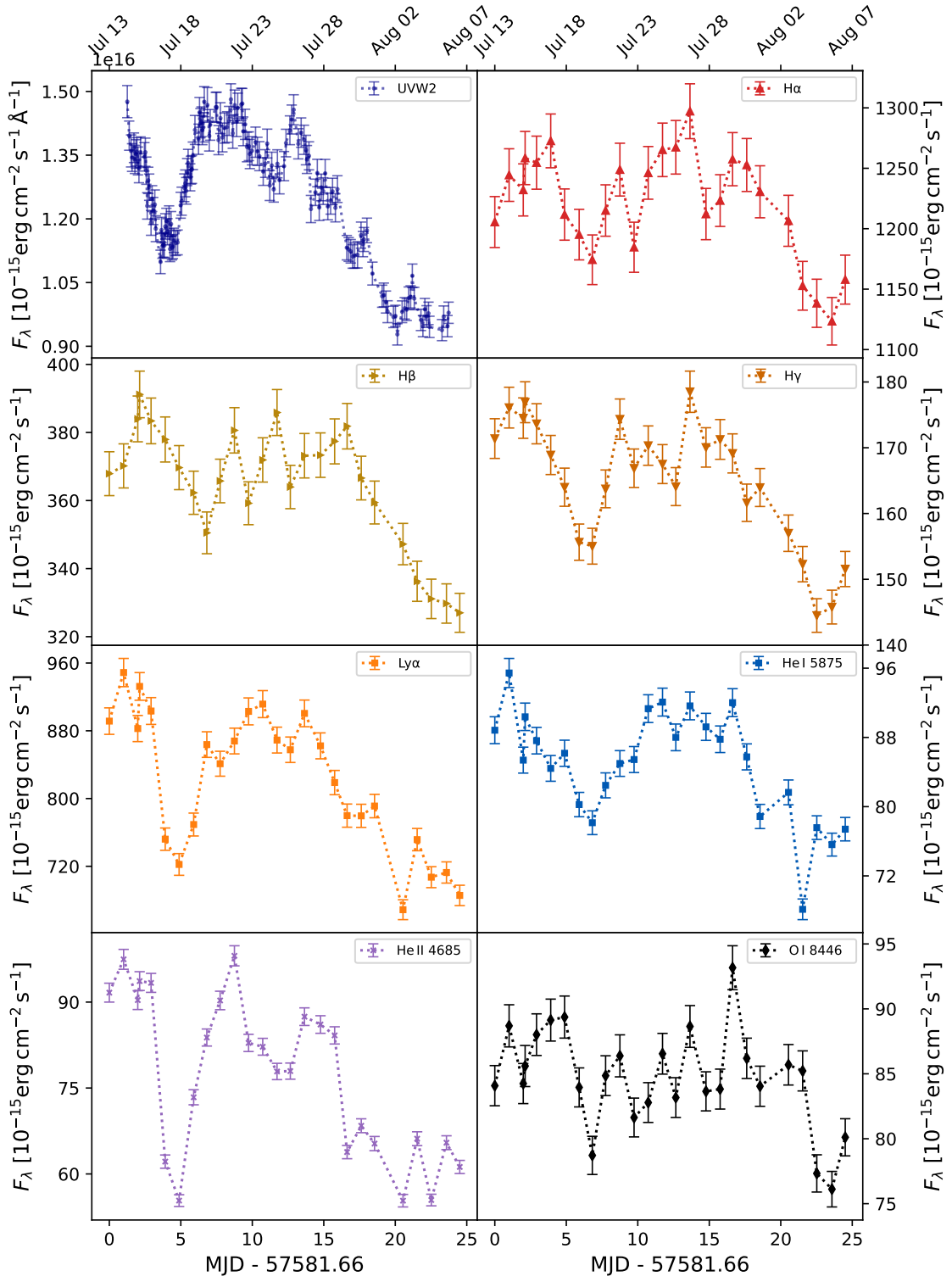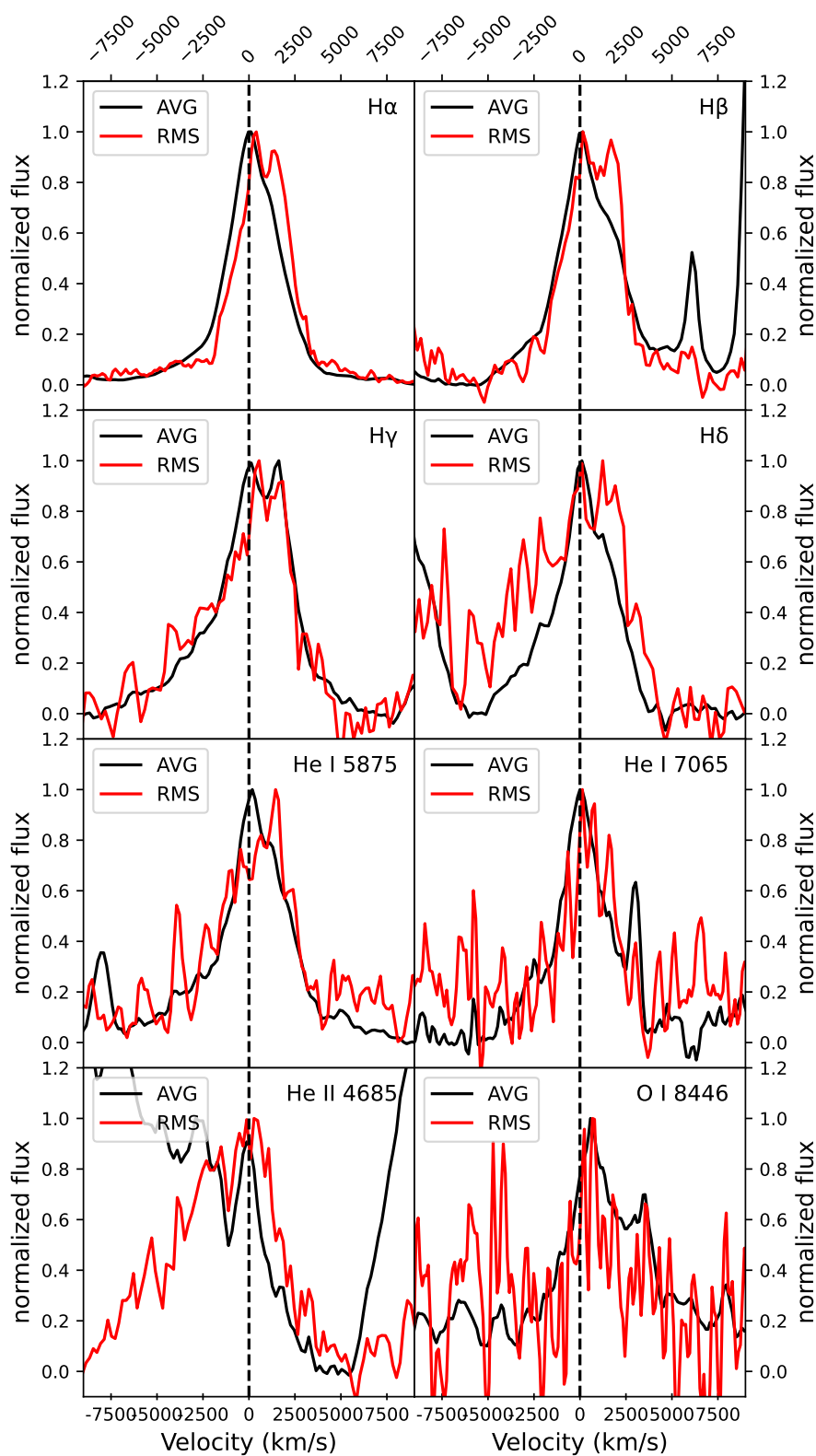
Figure 4.5: AVG RMS Spektrum

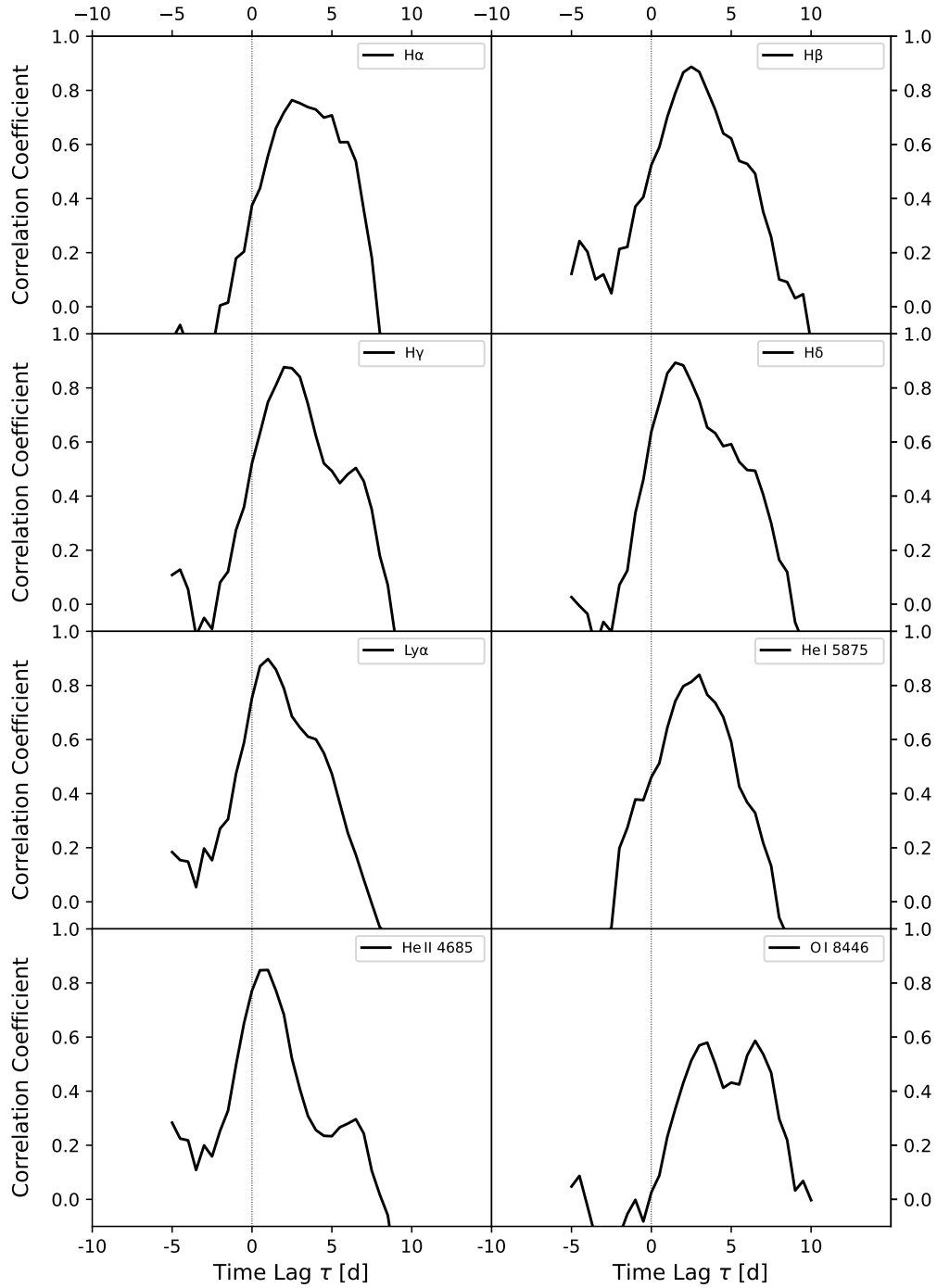# Normalized Line Profiles

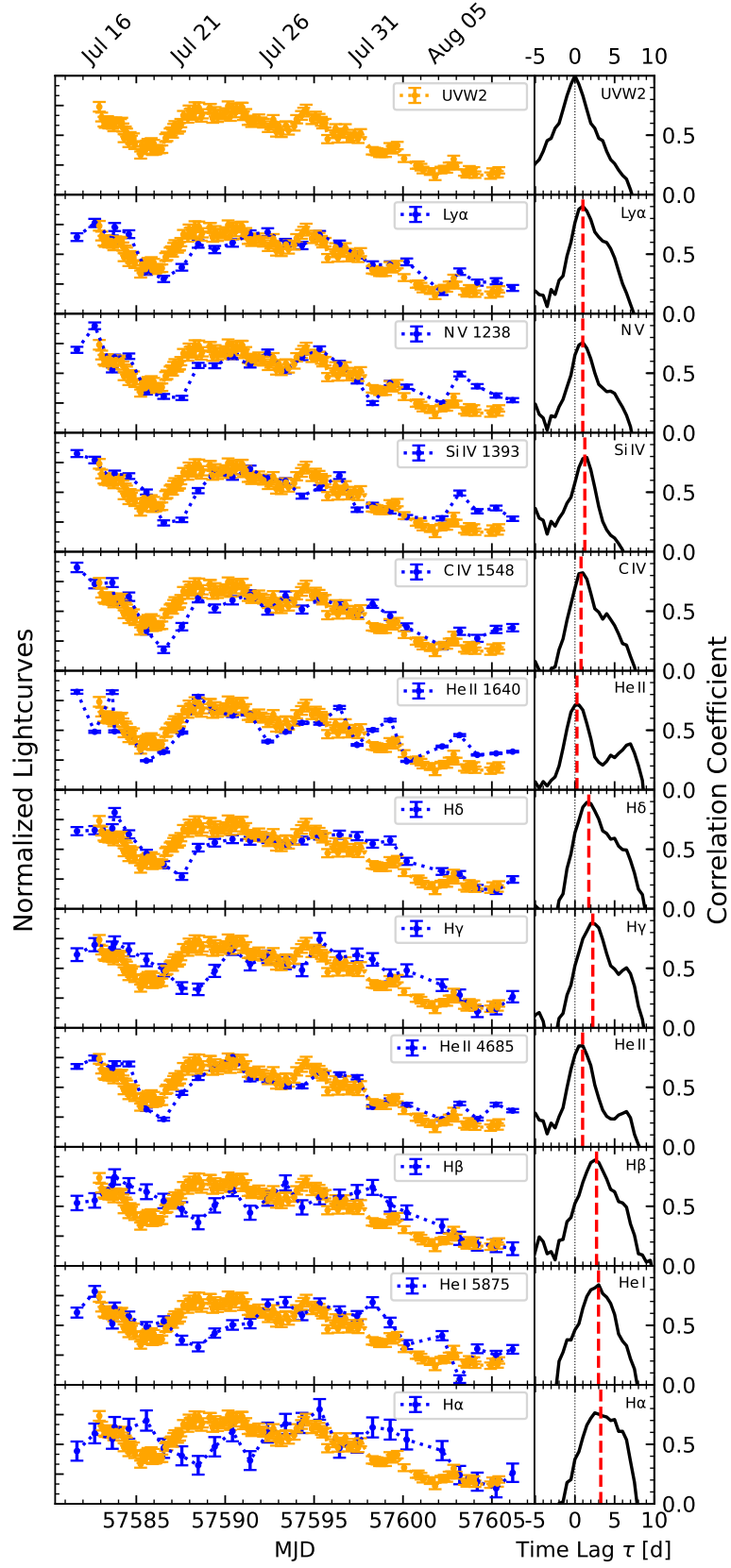Figure 4.6: AVG RMS Spektrum

Figure 4.7: AVG RMS Spektrum

Figure 4.8: AVG RMS Spektrum

5. Discussion

Bibliography

Anderson, Jay and Luigi R Bedin (2010). "An empirical pixel-based correction for imperfect cte. i. hst's advanced camera for surveys1". In: *Publications of the Astronomical Society of the Pacific* 122.895, p. 1035.

Antonucci, Robert (1993). "Unified models for active galactic nuclei and quasars". In: *Annual Review of Astronomy and Astrophysics* 31, pp. 473–521. DOI: 10. 1146/annurev.aa.31.090193.002353.

Beckmann, Volker and Chris Shrader (Feb. 2013). "The AGN phenomenon: Open issues". In: *Proceedings of Science.*

Bentz, Misty C and Sarah Katz (2015). "The AGN black hole mass database". In: *Publications of the Astronomical Society of the Pacific* 127.947, p. 67.

Bowen, I. S. (1934). "The excitation of the permitted O III nebular lines". In: *Publications of the Astronomical Society of the Pacific* 46.271, pp. 146–148.

Bowen, I. S. (Aug. 1947). "EXCITATION BY LINE COINCIDENCE". In: *Publications of the Astronomical Society of the Pacific* 59.349, p. 196. DOI: 10.1086/ 125951. URL: https://doi.org/10.1086/125951.

Cackett, E. M., M. C. Bentz, and E. Kara (2021). "Reverberation Mapping of Active Galactic Nuclei: From X-ray Corona to Dusty Torus". In: *iScience* 24.12, p. 102557. DOI: 10.1016/j.isci.2021.102557.

Cackett, Edward M et al. (2018). "Accretion disk reverberation with Hubble space telescope observations of NGC 4593: evidence for diffuse continuum lags". In: *The Astrophysical Journal* 857.1, p. 53.

Denney, Kelly D. et al. (Dec. 2006). "The mass of the black hole in the Seyfert 1 galaxy NGC 4593 from reverberation mapping". In: *Astrophysical Journal Letters* 653, pp. 152–158. DOI: 10.1086/508533.

Dexter, Jason and Eric Agol (Dec. 2010). "Quasar accretion disks are strongly inhomogeneous". In: *The Astrophysical Journal* 727.1, p. L24. ISSN: 2041-8213. DOI: 10.1088/2041-8205/727/1/l24. URL: http://dx.doi.org/10.1088/2041-8205/727/1/L24.

Garcia-Burillo, S. et al. (2019). "ALMA images the many faces of the NGC1068 torus and its surroundings". In: *Astronomy & Astrophysics* 632, A61. DOI: `10.1051/0004-6361/201936606`.

Gaskell, C. Martin and Bradley M. Peterson (Sept. 1987). "The Accuracy of Cross-Correlation Estimates of Quasar Emission-Line Region Sizes". In: 65, p. 1. DOI: `10.1086/191216`.

Goad, M. R., K. T. Korista, and A. J. Ruff (Nov. 2012). "The broad emission-line region: the confluence of the outer accretion disc with the inner edge of the dusty torus". In: *Monthly Notices of the Royal Astronomical Society* 426.4, pp. 3086–3111. ISSN: 0035-8711. DOI: `10.1111/j.1365-2966.2012.21808.x`. eprint: `https://academic.oup.com/mnras/article-pdf/426/4/3086/3319519/426-4-3086.pdf`. URL: `https://doi.org/10.1111/j.1365-2966.2012.21808.x`.

Grandi, S. A. (May 1980). "OI lambda 8446 emission in Seyfert 1 galaxies." In: 238, p. 10. DOI: `10.1086/157952`.

Horne, Keith et al. (2004). "Observational Requirements for High-Fidelity Reverberation Mapping". In: *Publications of the Astronomical Society of the Pacific* 116.819, p. 465.

McHardy, I. M. et al. (2017). "X-ray/UV/optical variability of NGC 4593 with Swift: Reprocessing of X-rays by an extended reprocessor". In: *Monthly Notices of the Royal Astronomical Society* 465.3, pp. 273–289. DOI: `10.1093/mnras/stw2719`.

McHardy, IM et al. (2018). "X-ray/UV/optical variability of NGC 4593 with Swift: reprocessing of X-rays by an extended reprocessor". In: *Monthly Notices of the Royal Astronomical Society* 480.3, pp. 2881–2897.

Mo, Houjun, Frank van den Bosch, and Simon White (2010). *Galaxy Formation and Evolution.* Cambridge University Press. ISBN: 9780521857932.

Mulchaey, John S. and Michael W. Regan (June 1997). "The Fueling of Nuclear Activity: II. The Bar Properties of Seyfert and Normal Galaxies". In: *The Astrophysical Journal Letters* 482.2, pp. L135–L138. DOI: `10.1086/310710`.

Netzer, H. and M. V. Penston (Feb. 1976). "Physical Conditions in Active Nuclei–II O I λ 8446 FLUORESCENCE". In: *Monthly Notices of the Royal Astronomical Society* 174.2, pp. 319–325. ISSN: 0035-8711. DOI: `10.1093/mnras/174.2.319`. eprint: `https://academic.oup.com/mnras/article-pdf/174/2/319/18325191/mnras174-0319.pdf`. URL: `https://doi.org/10.1093/mnras/174.2.319`.

Netzer, Hagai (2013). *The Physics and Evolution of Active Galactic Nuclei.* English. 1st ed. Cambridge: Cambridge University Press. ISBN: 9781107021518.

Ochmann, MW et al. (2024). "The transient event in NGC 1566 from 2017 to 2019-I. An eccentric accretion disk and a turbulent, disk-dominated broad-line region unveiled by double-peaked Ca II and O I lines". In: *Astronomy & Astrophysics* 686, A17.

Onken, C. A. et al. (2004). "Supermassive Black Holes in Active Galactic Nuclei. II. Calibration of the Black Hole Mass-Velocity Dispersion Relationship for Active Galactic Nuclei". In: *The Astrophysical Journal* 615, pp. 645–651. DOI: `10.1086/424655`.

Osterbrock, D. E. (Aug. 1977). "Spectrophotometry of Seyfert 1 galaxies." In: 215, pp. 733–745. DOI: `10.1086/155407`.

Osterbrock, D. E. (Oct. 1981). "Seyfert galaxies with weak broad H alpha emission lines". In: 249, pp. 462–470. DOI: `10.1086/159306`.

Osterbrock, Donald E. and Richard W. Pogge (1985). "The spectra of narrow-line Seyfert 1 galaxies". In: *The Astrophysical Journal* 297, pp. 166–176. DOI: `10.1086/163513`.

Peterson, B. M. (1993). "Reverberation Mapping of Active Galactic Nuclei". In: *Publications of the Astronomical Society of the Pacific* 105, pp. 247–268. DOI: `10.1086/133140`.

Peterson, B. M. et al. (1998). "Optical Continuum and Emission-Line Variability of Seyfert 1 Galaxies". In: *The Astrophysical Journal* 501, pp. 82–93. DOI: `10.1086/305813`.

Peterson, B. M. et al. (2004). "Central Masses and Broad-Line Region Sizes of Active Galactic Nuclei. II. A Homogeneous Analysis of a Large Reverberation-Mapping Database". In: *The Astrophysical Journal* 613, pp. 682–699. DOI: `10.1086/423269`.

Peterson, Bradley M. (1997). *An Introduction to Active Galactic Nuclei*. Cambridge University Press. ISBN: 0521473489.

Peterson, Bradley M. (2011). *Masses of Black Holes in Active Galactic Nuclei: Implications for NLS1s*. arXiv: `1109.4181` [`astro-ph.CO`]. URL: `https://arxiv.org/abs/1109.4181`.

Rees, Martin J. (Jan. 1984). "Black Hole Models for Active Galactic Nuclei". In: 22, pp. 471–506. DOI: `10.1146/annurev.aa.22.090184.002351`.

Ricci, Claudio and Benny Trakhtenbrot (2023). "Changing-look active galactic nuclei". In: *Nature Astronomy* 7.11, pp. 1282–1294.

Rodriguez-Pascual, PM et al. (1997). "Steps toward determination of the size and structure of the broad-Line region in active galactic nuclei. IX. Ultraviolet ob-

servations of fairall 9". In: *The Astrophysical Journal Supplement Series* 110.1, p. 9.

Runco, Jordan (2015). "Frequency of Seyfert Type Transitions in a Sample of 102 Local Active Galactic Nuclei". In.

Seyfert, Carl K. (1943). "Nuclear Emission in Spiral Nebulae". In: *The Astrophysical Journal* 97, pp. 28–40. DOI: 10.1086/144488.

Shakura, N. I. and R. A. Sunyaev (1973). "Black holes in binary systems. Observational appearance". In: *Astronomy and Astrophysics* 24, pp. 337–355.

SIMBAD (2025). *NGC4593*. URL: https://simbad.u-strasbg.fr/simbad/sim-id?Ident=NGC4593 (visited on 06/10/2025).

Skrutskie, M. F. and et al. (2006). "The Two Micron All Sky Survey (2MASS)". In: *The Astronomical Journal* 131, pp. 1163–1183. DOI: 10.1086/498708.

Space Telescope Science Institute (2025). *STIS Instrument Handbook: Gratings*. URL: https://hst-docs.stsci.edu/stisihb/chapter-13-spectroscopic-reference-material/13-3-gratings (visited on 05/12/2025).

Ulrich, Marie-Helene, Laura Maraschi, and C Megan Urry (1997). "Variability of active galactic nuclei". In: *Annual Review of Astronomy and Astrophysics* 35.1, pp. 445–502.

Urry, C. Megan and Paolo Padovani (1995). "Unified Schemes for Radio-Loud Active Galactic Nuclei". In: *Publications of the Astronomical Society of the Pacific* 107.715, pp. 803–845. DOI: 10.1086/133630.

Véron-Cetty, M-P and Philippe Véron (2010). "A catalogue of quasars and active nuclei". In: *Astronomy and Astrophysics* 518, A10.